# Chapter 4

# Beam Dynamics and Beam Related Systematic Errors

## 4.1 Introduction

In this chapter we discuss the behavior of a beam in a weak-focusing betatron, and the features of the injection of a bunched beam that are important in the determination of $\omega_a$. We also discuss the corrections to the measured frequency $\omega_a$ that come from the vertical betatron motion, and the fact that not all muons are at the magic momentum (central radius) in the storage ring. The final section of this chapter discusses the systematic errors that come from the pion and muon beamlines.

## 4.2 The Weak Focusing Betatron

The behavior of the beam in the $(g-2)$ storage ring directly affects the measurement of $a_\mu$. Since the detector acceptance for decay electrons depends on the radial coordinate of the muon at the point where it decays, coherent radial motion of the stored beam can produce an amplitude modulation in the observed electron time spectrum. Resonances in the storage ring can cause particle losses, thus distorting the observed time spectrum, and must be avoided when choosing the operating parameters of the ring. Care is taken in setting the frequency of coherent radial beam motion, the "coherent betatron oscillation" (CBO) frequency, which lies close to the second harmonic of $f_a = \omega_a/(2\pi)$. If $f_{\text{CBO}}$ is too close to $2f_a$, the beat frequency, $f_- = f_{CBO} - f_a$, complicates the extraction of $f_a$ from the data, and can introduce a significant systematic error.

A pure quadrupole electric field provides a linear restoring force in the vertical direction, and the combination of the (defocusing) electric field and the central magnetic field provides a linear restoring force in the radial direction. The $(g-2)$ ring is a weak focusing ring[1, 2, 3] with the field index

$$n = \frac{\kappa R_0}{\beta B_0}, \tag{4.1}$$

where $\kappa$ is the electric quadrupole gradient, $B_0$ is the magnetic field strength, $R_0$ is the magic radius $\equiv 7112$ mm, and $\beta$ is the relativistic velocity of the muon beam. For a ring

with a uniform vertical dipole magnetic field and a uniform quadrupole field that provides vertical focusing covering the full azimuth, the stored particles undergo simple harmonic motion called betatron oscillations, in both the radial and vertical dimensions.

The horizontal and vertical motion are given by

$$x = x_e + A_x \cos(\nu_x \frac{s}{R_0} + \delta_x) \quad \text{and} \quad y = A_y \cos(\nu_y \frac{s}{R_0} + \delta_y), \tag{4.2}$$

where $s$ is the arc length along the trajectory. The horizontal and vertical tunes are given by

$$\nu_x = \sqrt{1-n} \quad \text{and} \quad \nu_y = \sqrt{n}. \tag{4.3}$$

Several $n$ - values were used in E821 for data acquisition: $n = 0.137$, $0.142$ and $0.122$. The horizontal and vertical betatron frequencies are given by

$$f_x = f_C \sqrt{1-n} \simeq 0.929 f_C \quad \text{and} \quad f_y = f_C \sqrt{n} \simeq 0.37 f_C, \tag{4.4}$$

where $f_C$ is the cyclotron frequency and the numerical values assume that $n = 0.137$. The corresponding betatron wavelengths are $\lambda_{\beta_x} = 1.08(2\pi R_0)$ and $\lambda_{\beta_y} = 2.7(2\pi R_0)$. It is important that the betatron wavelengths are not simple multiples of the circumference, as this minimizes the ability of ring imperfections and higher multipoles to drive resonances that would result in particle losses from the ring.

Table 4.1: Frequencies in the $(g-2)$ storage ring, assuming that the quadrupole field is uniform in azimuth and that $n = 0.137$.

| Quantity | Expression | Frequency [MHz] | Period [$\mu$s] |
|----------|------------|-----------------|-----------------|
| $f_a$ | $\frac{e}{2\pi mc} a_\mu B$ | 0.228 | 4.37 |
| $f_C$ | $\frac{v}{\pi R_0}$ | 6.7 | 0.149 |
| $f_x$ | $\sqrt{1-n} f_c$ | 6.23 | 0.160 |
| $f_y$ | $\sqrt{n} f_c$ | 2.48 | 0.402 |
| $f_{CBO}$ | $f_c - f_x$ | 0.477 | 2.10 |
| $f_{VW}$ | $f_c - 2f_y$ | 1.74 | 0.574 |

As a reminder, the muon frequency, $\omega_a$ is determined by the average magnetic field weighted by the muon distribution and the magnetic anomaly:

$$\vec{\omega}_a = -\frac{Qe}{m} \left[ a_\mu \vec{B} - \left( a_\mu - \left( \frac{mc}{p} \right)^2 \right) \frac{\vec{\beta} \times \vec{E}}{c} \right]. \tag{4.5}$$

The field index also determines the angular acceptance of the ring. The maximum horizontal and vertical angles of the muon momentum are given by

$$\theta^x_{\max} = \frac{x_{\max} \sqrt{1-n}}{R_0}, \quad \text{and} \quad \theta^y_{\max} = \frac{y_{\max} \sqrt{n}}{R_0}, \tag{4.6}$$

where $x_{\max}, y_{\max} = 45$ mm is the radius of the storage aperture. For a betatron amplitude $A_x$ or $A_y$ less than 45 mm, the maximum angle is reduced, as can be seen from the above equations.

## 4.3   Weak Focusing with Discrete Quadrupoles

For a ring with discrete quadrupoles, the focusing strength changes as a function of azimuth, and the equation of motion looks like an oscillator whose spring constant changes as a function of azimuth $s$. The motion is described by

$$x(s) = x_e + A\sqrt{\beta(s)}\cos(\psi(s) + \delta), \tag{4.7}$$

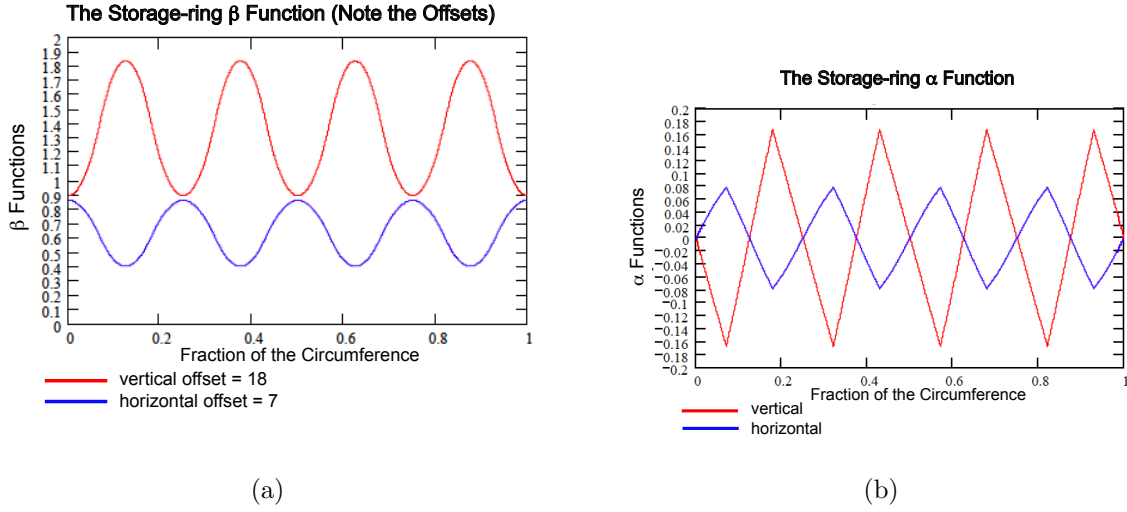where $\beta(s)$ is one of the three Courant-Snyder parameters.[2]





(a)                                                                        (b)

Figure 4.1: (a) The horizontal (radial) and vertical beta functions for the E821 lattice. Note the scale offset. (b) The horizontal (radial) and vertical alpha functions for the E821 lattice. The $n$-value is 0.134 for both. (From Ref. [9]

The layout of the storage ring is shown in Figure 4.2(a). The four-fold symmetry of the quadrupoles was chosen because it provided quadrupole-free regions for the kicker, tracking chambers, fiber monitors, and trolley garage; but the most important benefit of four-fold symmetry is to reduce the peak-to-peak betatron oscillation amplitudes, with $\sqrt{\beta_{\max}/\beta_{\min}} = 1.03$. The beta and alpha functions for the $(g-2)$ storage ring [9] are shown in Fig. 4.1.

Resonances in the storage ring will occur if $L\nu_x + M\nu_y = N$, where $L$, $M$ and $N$ are integers, which must be avoided in choosing the operating value of the field index. These resonances form straight lines on the tune plane shown in Figure 4.2(b), which shows resonance lines up to fifth order. The operating point lies on the circle $\nu_x^2 + \nu_y^2 = 1$.

The detector acceptance depends on the radial position of the muon when it decays, so that any *coherent* radial beam motion will amplitude modulate the decay $e^\pm$ distribution. This can be understood by examining Fig. 4.3. A narrow bunch of muons starts its radial betatron oscillation at the point $s = 0$. The circumference of the ring is $2\pi\rho$ so the $x$-axis shows successive revolutions around the ring. The radial betatron wavelength is longer than the circumference $2\pi\rho$. The rate at which the muon bunch moves toward and then away from the detector is given by $f_{CBO} = f_C - f_x$. The CBO wavelength is slightly over 14 revolutions of the ring.
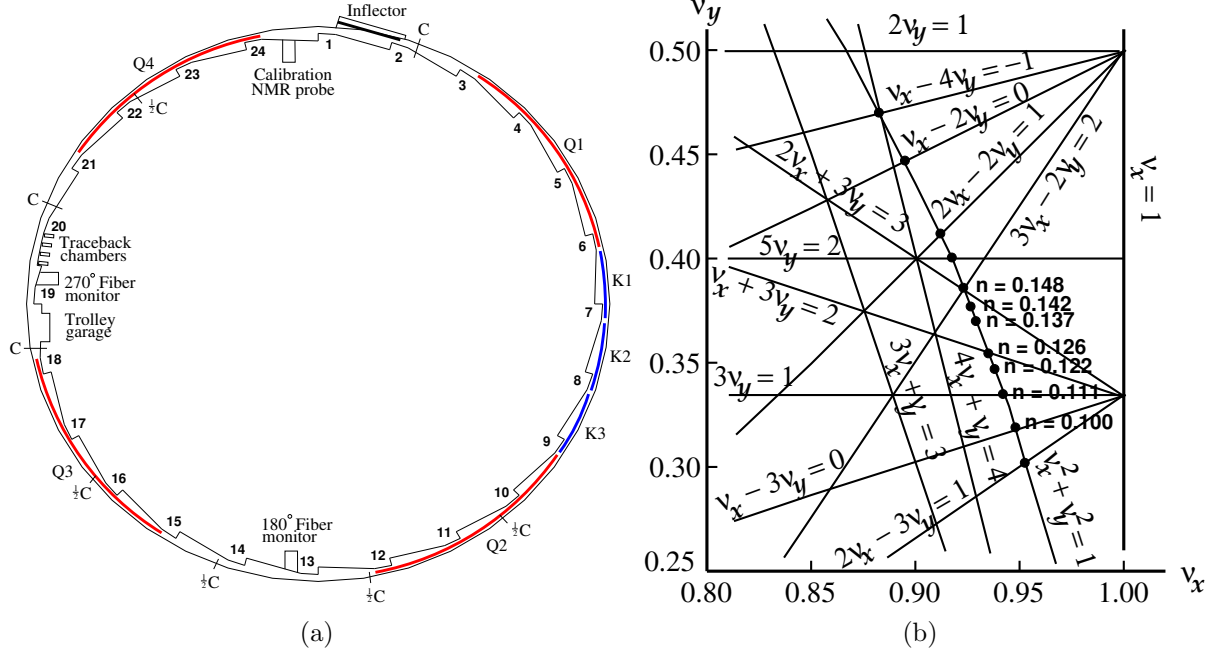
Figure 4.2: (a) The layout of the storage ring. (b)The tune plane, showing the three operating points used during our three years of E821 running.

The presence of the CBO was first discovered in E821 from a plot that showed an azimuthal variation in the value of $a_\mu$ shown in Fig. 4.4(a). When the CBO is included, this azimuthal dependence disappears. Because the CBO wavelength is only slightly greater than the circumference, its effect almost washes out when all detectors are added together. Adding all detectors together was one of the techniques used in E821 to eliminate CBO effect. However, the four-fold symmetry of the ring was broken by the kicker plates that covered one section of the ring, so the cancellation was not perfect, but good enough. This will most likely not be true in E989, so it is important to minimize the CBO effects. See Chapter 13 for further discussion. Since some detectors saw more injection flash than others, this meant that data at times earlier than around 40 $\mu$s was discarded in those analyses. Other analyzers included the CBO and were able to use data from the "quiet" detectors at earlier times.

The principal frequency will be the "Coherent Betatron Frequency,"

$$f_{\text{CBO}} = f_C - f_x = (1 - \sqrt{1-n})f_C \simeq 470 \text{ kHZ}, \tag{4.8}$$

which is the frequency at which a single fixed detector sees the beam coherently moving back and forth radially. This CBO frequency is close to the second harmonic of the $(g-2)$ frequency, $f_a = \omega_a/2\pi \simeq 228$ Hz.

An alternative way of thinking about the CBO motion is to view the ring as a spectrometer where the inflector exit is imaged at each successive betatron wavelength, $\lambda_{\beta_x}$. In principle, an inverted image appears at half a betatron wavelength; but the radial image is spoiled by the $\pm 0.3\%$ momentum dispersion of the ring. A given detector will see the beam move radially with the CBO frequency, which is also the frequency at which the horizontal
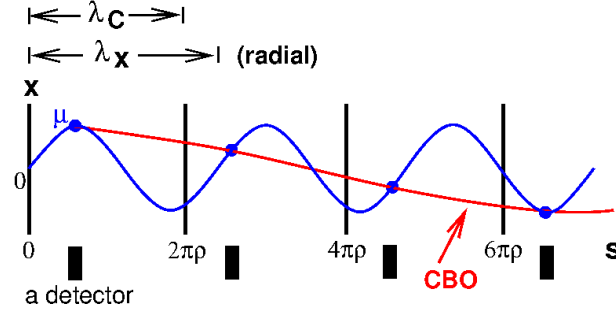
Figure 4.3: A cartoon of the coherent betatron motion (CBO). The radial CBO oscillation is shown in blue for 3 successive betatron wavelengths, the cyclotron wavelength (the circumference) is marked by the black vertical lines. One detector location is shown. Since the radial betatron wavelength is larger than the circumference, the detector sees the bunched beam slowly move closer and then further away. The frequency that the beam appears to move in and out is $f_{CBO}$ .
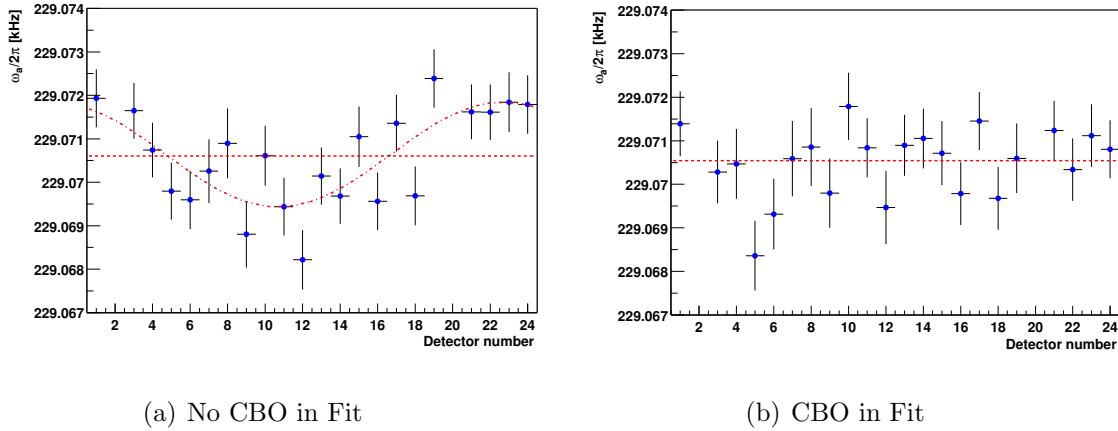


(a) No CBO in Fit                                        (b) CBO in Fit

Figure 4.4: The dependence of the extracted value of $a_\mu$ vs. detector number. (a)With no CBO in the fit function. (b) With CBO included in the fit function.

waist precesses around the ring. The vertical waist betatron wavelength is only 2.7 turns, and disappears rather quickly. A number of frequencies in the ring are tabulated in Table 4.1

The CBO frequency and its sidebands are clearly visible in the Fourier transform to the residuals from a fit to the five-parameter fitting function Equation 3.18, and are shown in Figure 4.5. The vertical waist frequency is barely visible. In 2000, the quadrupole voltage was set such that the CBO frequency was uncomfortably close to the second harmonic of $f_a$, thus placing the difference frequency $f_- = f_{CBO} - f_a$ next to $f_a$. This nearby sideband forced us to work very hard to understand the CBO and how its related phenomena affect the value of $\omega_a$ obtained from fits to the data. In 2001, we carefully set $f_{CBO}$ at two different values, one well above, the other well below $2f_a$, which greatly reduced this problem.
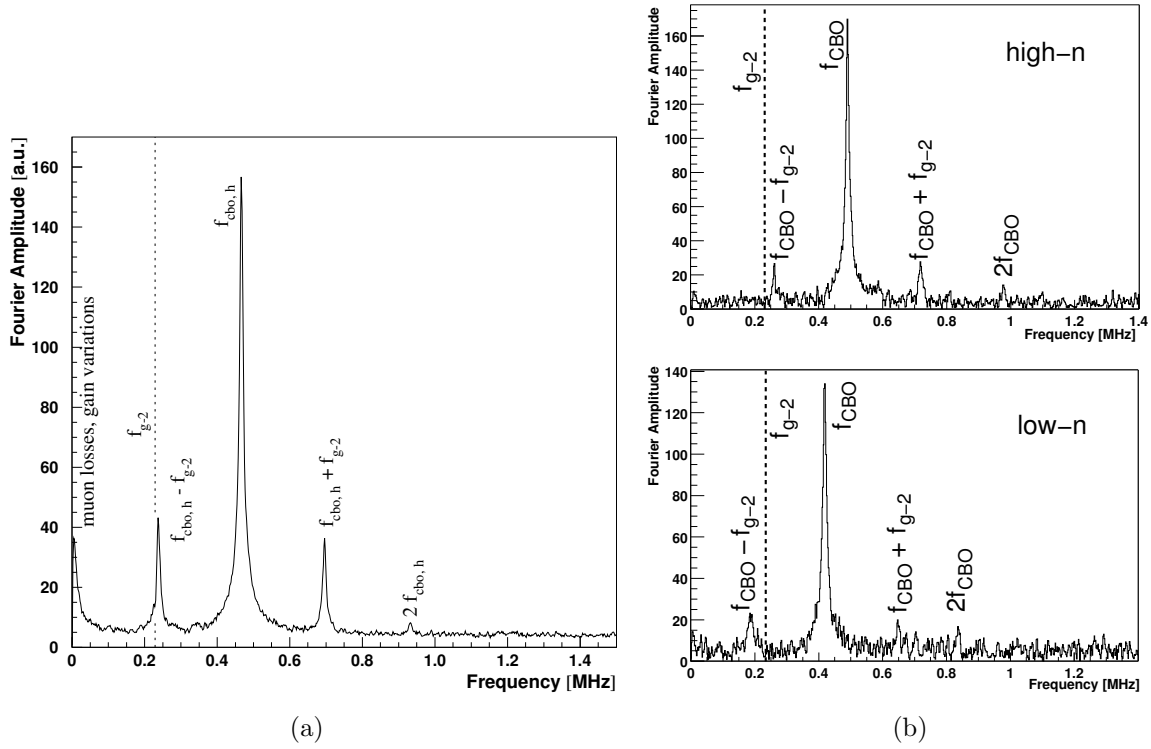
Figure 4.5: The Fourier transform to the residuals from a fit to the five-parameter function, showing clearly the coherent beam frequencies. (a) is from 2000, when the CBO frequency was close to $2\omega_a$, and (b) shows the Fourier transform for the two n-values used in the 2001 run period.

### 4.3.1   Monitoring the Beam Profile

Knowledge of the distribution of stored beam in the storage ring is necessary for several important corrections to the measured muon spin rotation frequency. There are three tools available to determine this distribution:

1. Tracking chambers (see Chapter 19) that measure the trajectories of the decay positrons, and reconstruct the vertical and horizontal spacial distribution of stored muons.

2. Measurement of the beam de-bunching after injection into the ring; called the "fast rotation analysis", which is discussed below.

3. Fiber beam monitors, which consist of $x$ and $y$ arrays of 0.5 mm scintillating fibers that can be inserted into the storage region to measure the central part of the muon distribution (see Chapter 20).

Because of the limited momentum acceptance of the Recycler Ring, the minimum proton bunch width is 120 ns, as is shown in Fig. 7.5. In E821 the beam had an rms $\sim$ 25 ns. These beam widths should be compared to the cyclotron period of the storage ring of 149 ns. We

first discuss the E821 case, with its narrow beam. The momentum distribution of stored muons produces a corresponding distribution in radii of curvature. The distributions depend on the phase-space acceptance of the ring, the phase space of the beam at the injection point, and the kick given to the beam at injection. The narrow 18 mm horizontal aperture of the E821 inflector magnet restricts the stored momentum distribution to about ±0.15%. As the muons circle the ring, the muons at smaller radius (lower momentum) eventually pass those at larger radius repeatedly after multiple transits around the ring, and the bunch structure largely disappears after 60 $\mu$s . This de-bunching can be seen in the E821 data in Figure 4.6 where the signal from a single detector is shown at two different times following injection. The bunched beam is seen very clearly in the left figure, with the 149 ns cyclotron period being obvious. The slow amplitude modulation comes from the $(g-2)$ precession. By 36 $\mu$s the beam has largely de-bunched.
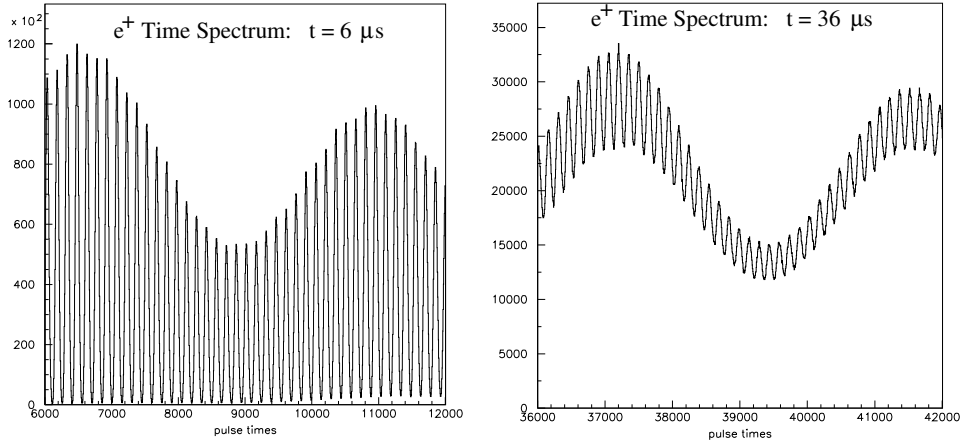


Figure 4.6: The time spectrum of a single E821 calorimeter soon after injection. The spikes are separated by the cyclotron period of 149 ns. The time width of the beam at injection was $\sigma \simeq 23$ ns.

Only muons with orbits centered at the central radius have the "magic" momentum, so knowledge of the momentum distribution, or equivalently the distribution of equilibrium radii, is important in determining the correction to $\omega_a$ caused by the radial electric field used for vertical focusing. Two methods of obtaining the distribution of equilibrium radii from the beam debunching were employed in E821. One method uses a model of the time evolution of the bunch structure. A second, alternative procedure uses modified Fourier techniques[8].

We discuss the former method, which was descended from the third CERN experiment, and show a preliminary study that demonstrates the ability to use this method to determine the distribution of equilibrium radii in E989. The initial bunched beam is modeled as an ensemble of particles having an unknown frequency distribution and a narrow time spread. The model assumes that every time slice of the beam has the same frequency profile but the time width is left as a fit parameter, as is the exact injection time. The distribution of angular frequencies will cause the bunched beam to spread out around the ring over time, in a manner that depends uniquely on the momentum distribution. In particular,

the time evolution of any finite frequency slice is readily specified. A given narrow bin of frequencies contributes linearly to the time spectrum. The total time spectrum is a sum over many of these frequency components, with amplitudes that can be determined using $\chi^2$ minimization. The momentum distribution is then determined from the frequency distribution (or equivalently, from the radial distribution) by

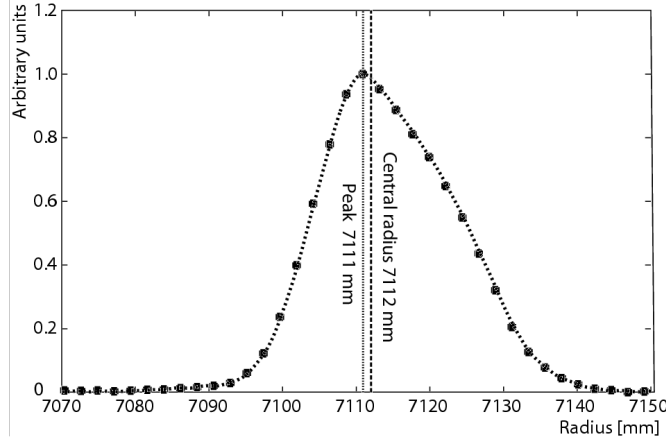$$\frac{p - p_0}{p_0} = (1 - n)\left(\frac{R - R_0}{R_0}\right). \tag{4.9}$$



Figure 4.7: The distribution of equilibrium radii obtained from the beam de-bunching. The solid circles are from a de-bunching model fit to the data, and the dotted curve is obtained from a modified Fourier analysis.

The result of the fast-rotation analysis from one of the E821 running periods is shown in Fig. 4.7. The smooth curve is obtained from the modified Fourier transform analysis. The peak of the distribution lies below the nominal magic radius of 7112 mm but the mean is somewhat larger, $7116 \pm 1$ mm for this run period. The rms width is about 10 mm, and the two methods give equivalent results.

Early in the planning for E989, it became clear that the Recycler beam would be much wider than that produced by the BNL AGS. A preliminary beam profile, shown in Fig. 4.8(a), was used to determine whether the fast rotation analysis could be used for such a wide beam. The equilibrium distribution for the simulation was chosen to be Gaussian, with a mean of 7112 mm and width 14.2 mm. The time structure seen by a single detector is shown in Fig. 4.8(b), which can be compared to Fig. 4.6. The distribution of equilibrium radii obtained from the analysis of the debunching is shown in Fig. 4.8(c). The input mean was recovered in the analysis. Several questions will be addressed in future studies: What is the connection between the $t_0$ phase and the distribution of equilibrium radii? What happens if the equilibrium radius is changed significantly by beam scraping after injection? Would this be easier to detect and correct for with a narrower pulse?

While the scintillating-fiber monitors were not that useful in measuring the beam profile, they were extremely useful in measuring the various frequencies in the muon beam motion. The pulse height from a single fiber varies as the beam oscillates across it, and show clearly the vertical and horizontal tunes as expected. In Figure 4.9, the horizontal beam centroid
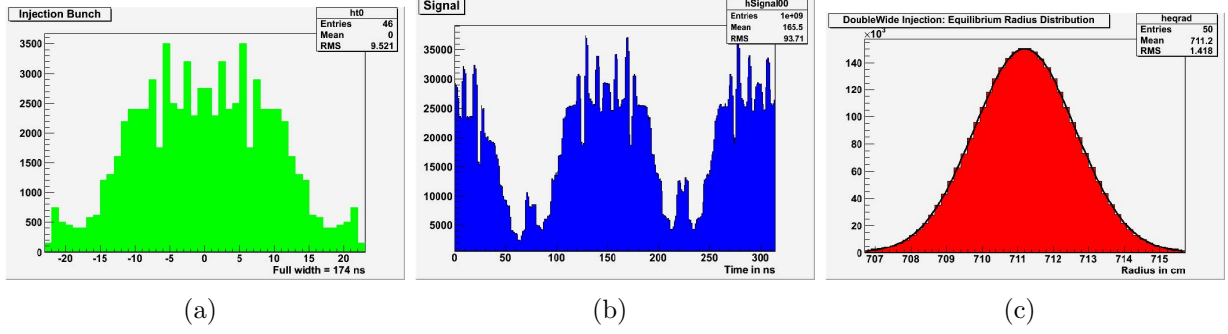
Figure 4.8: Simulations of a temporally wide beam. (a) An early version of the Recycler output beam. (b) The time spectrum shortly after injection, which can be compared with the left-hand E821 calorimeter after injection shown Fig. 4.6. (c) The distribution of equilibrium radii extracted from the debunching in these simulated data.

motion is shown, with the quadrupoles powered asymmetrically during scraping, and then symmetrically after scraping. A Fourier transform of the latter signal shows the expected frequencies, including the cyclotron frequency of protons stored in the ring.
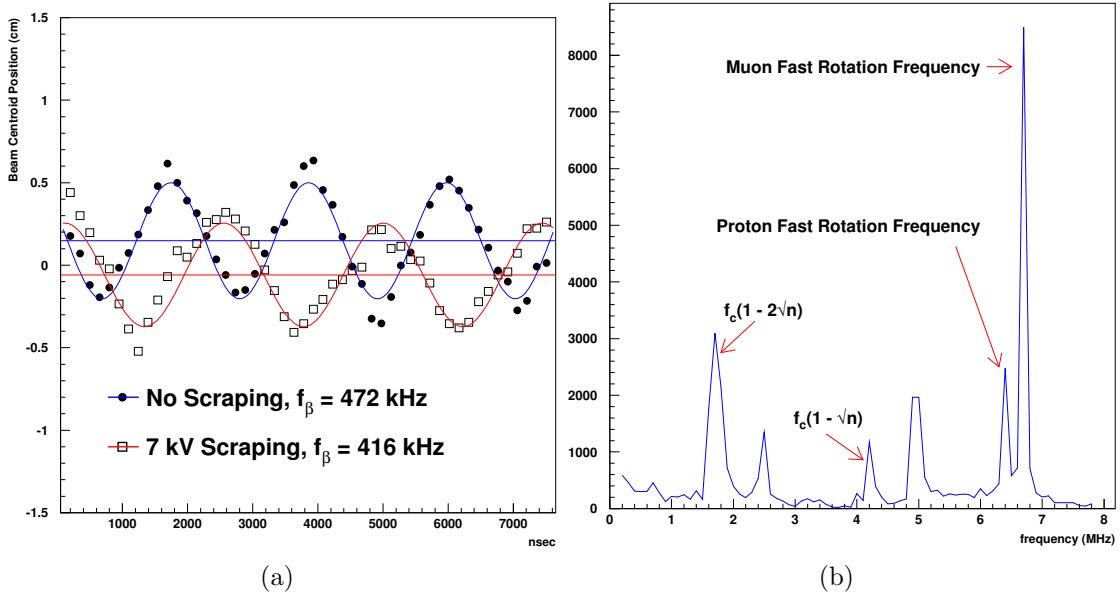


Figure 4.9: (a) The horizontal beam centroid motion with beam scraping and without, using data from the scintillating fiber hodoscopes; note the tune change between the two. (b) A Fourier transform of the pulse from a single horizontal fiber, which shows clearly the vertical waist motion, as well as the vertical tune. The presence of stored protons is clearly seen in this frequency spectrum.

## 4.4 Corrections to $\omega_a$: Pitch and Radial Electric Field

In the simplest case, in the absence of an electric field and when the velocity is perpendicular to the magnetic field, the rate at which the spin turns relative to the momentum is given by

$$\omega_a = \omega_S - \omega_C = -\left(\frac{g-2}{2}\right)\frac{Qe}{m}B = -a\frac{Qe}{m}B \qquad (4.10)$$

The spin equation modified by the presence of an electric field was introduced earlier, with the assumption that the velocity is transverse to the magnetic field. In the approximation that all muons are at the magic momentum, $\gamma_{\text{magic}} = p_{\text{magic}}/m\beta$, the electric field does not affect the spin rotation.

At the current and proposed levels of experimental precision, corrections for the approximations that the velocity is perpendicular to the field and that all muons are at the magic momentum must be made; the vertical betatron motion must be included, and the storage ring momentum acceptance of $\pm 0.5\%$ means that the muons have a range of momenta not quite at the magic momentum. Corrections to the measured value for $\omega_a$ from these two effects were made to the data in E821 after the data were un-blinded. In the 2001 data set, the electric field correction for the low $n$-value data set was $+0.47 \pm 0.05$ ppm. The pitch correction was $+0.27 \pm 0.04$ ppm. These are the only corrections made to the $\omega_a$ data.

We sketch the derivation for E821 and E989 below[4]. For a general derivation the reader is referred to References [6, 7].

For the more general case where $\vec{\beta} \cdot \vec{B} \neq 0$ and $\vec{E} \neq 0$, the cyclotron rotation frequency becomes:

$$\vec{\omega}_C = -\frac{Qe}{m}\left[\frac{\vec{B}}{\gamma} - \frac{\gamma}{\gamma^2 - 1}\left(\frac{\vec{\beta} \times \vec{E}}{c}\right)\right], \qquad (4.11)$$

and the spin rotation frequency becomes[5]

$$\vec{\omega}_S = -\frac{Qe}{m}\left[\left(\frac{g}{2} - 1 + \frac{1}{\gamma}\right)\vec{B} - \left(\frac{g}{2} - 1\right)\frac{\gamma}{\gamma + 1}(\vec{\beta} \cdot \vec{B})\vec{\beta} - \left(\frac{g}{2} - \frac{\gamma}{\gamma + 1}\right)\left(\frac{\vec{\beta} \times \vec{E}}{c}\right)\right]. \qquad (4.12)$$

Substituting for $a_\mu = (g_\mu - 2)/2$, we find that the spin difference frequency is

$$\vec{\omega}_{diff} = \vec{\omega}_S - \vec{\omega}_C = -\frac{Qe}{m}\left[a_\mu\vec{B} - a_\mu\left(\frac{\gamma}{\gamma + 1}\right)(\vec{\beta} \cdot \vec{B})\vec{\beta} - \left(a_\mu - \frac{1}{\gamma^2 - 1}\right)\frac{\vec{\beta} \times \vec{E}}{c}\right]. \qquad (4.13)$$

Strictly speaking, the rate of change of the angle between the spin and the momentum vectors, $|\vec{\omega}_a|=$'precession frequency', is equal to $|\vec{\omega}_{diff}|$ only if $\vec{\omega}_S$ and $\vec{\omega}_C$ are parallel. For the E821 and E989 experiments, the angle between $\vec{\omega}_S$ and $\vec{\omega}_C$ is always small and the rate of oscillation of $\vec{\beta}$ out of pure circular motion is fast compared to $\omega_a$, allowing us in the following discussion the make the approximation that $\vec{\omega}_a \simeq \vec{\omega}_{diff}$. More general calculations, where this approximation is not made, are found in References [6, 7]. In the E821 and E989 limits, the results presented here are the same as in the References.

If $\vec{\beta} \cdot \vec{B} = 0$, the angle between the momentum and spin reduces to the previously introduced expression

$$\vec{\omega}_a \simeq \vec{\omega}_{diff} = -\frac{Qe}{m}\left[a_\mu \vec{B} - \left(a_\mu - \frac{1}{\gamma^2 - 1}\right)\frac{\vec{\beta} \times \vec{E}}{c}\right]. \tag{4.14}$$

For $\gamma_{\mathrm{magic}} = 29.3$ ($p_\mu = 3.09$ GeV/$c$), the second term vanishes and the electric field does not contribute to the spin precession. In that case, the spin precession is independent of muon momentum; *all* muons precess at the same rate. Because of the high uniformity of the B-field, a precision knowledge of the stored beam trajectories in the storage region is not required.

First we calculate the effect of the electric field due to muons not exactly at $\gamma_{\mathrm{magic}} = 29.3$, for the moment neglecting the $\vec{\beta} \cdot \vec{B}$ term. If the muon momentum is different from the magic momentum, the precession frequency is given by

$$\omega'_a = \omega_a\left[1 - \beta\frac{E_r}{cB_y}\left(1 - \frac{1}{a_\mu\beta^2\gamma^2}\right)\right], \tag{4.15}$$

where $\omega_a = -a\frac{Qe}{m}B$. Using $p = \beta\gamma m = (p_m + \Delta p)$, after some algebra one finds

$$\frac{\omega'_a - \omega_a}{\omega_a} = \frac{\Delta\omega_a}{\omega_a} = -2\frac{\beta E_r}{cB_y}\left(\frac{\Delta p}{p_m}\right). \tag{4.16}$$

Thus the effect of the radial electric field reduces the observed frequency from the simple frequency $\omega_a$ given in Equation 4.13. Now

$$\frac{\Delta p}{p_m} = (1 - n)\frac{\Delta R}{R_0} = (1 - n)\frac{x_e}{R_0}, \tag{4.17}$$

where $x_e$ is the muon's equilibrium radius of curvature relative to the central orbit. The electric quadrupole field is

$$E = \kappa x = \frac{n\beta cB_y}{R_0}x. \tag{4.18}$$

We obtain

$$\frac{\Delta\omega}{\omega} = -2n(1 - n)\beta^2\frac{xx_e}{R_0^2}, \tag{4.19}$$

so clearly the effect of muons not at the magic momentum is to lower the observed frequency. For a quadrupole focusing field plus a uniform magnetic field, the time average of $x$ is just $x_e$, so the electric field correction is given by

$$C_E = \frac{\Delta\omega}{\omega} = -2n(1 - n)\beta^2\frac{\langle x_e^2\rangle}{R_0^2}, \tag{4.20}$$

where $\langle x_e^2\rangle$ is determined from the fast-rotation analysis (see Figure 4.6). The uncertainty on $\langle x_e^2\rangle$ is added in quadrature with the uncertainty in the placement of the quadrupoles of $\delta R = \pm 0.5$ mm ($\pm 0.01$ ppm), and with the uncertainty in the mean vertical position of the beam, $\pm 1$ mm ($\pm 0.02$ ppm). For the low-$n$ 2001 sub-period, $C_E = 0.47 \pm 0.054$ ppm.
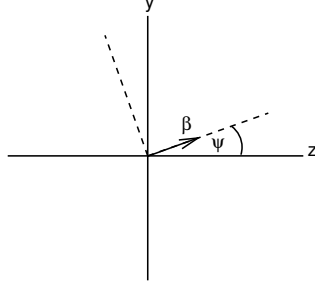
Figure 4.10: The coordinate system of the pitching muon. The angle $\psi$ varies harmonically. The vertical direction is $\hat{y}$ and $\hat{z}$ is the azimuthal (beam) direction.

The betatron oscillations of the stored muons lead to $\vec{\beta} \cdot \vec{B} \neq 0$. Since the $\vec{\beta} \cdot \vec{B}$ term in Equation 4.12 is quadratic in the components of $\vec{\beta}$, its contribution to $\vec{\omega}_S$ will not generally average to zero. Thus the spin precession frequency has a small dependence on the betatron motion of the beam. It turns out that the only significant correction comes from the vertical betatron oscillation; therefore it is called the pitch correction (see Equation 4.13). As the muons undergo vertical betatron oscillations, the "pitch" angle between the momentum and the horizontal (see Figure 4.10) varies harmonically as $\psi = \psi_0 \cos \omega_y t$, where $\omega_y$ is the vertical betatron frequency $\omega_y = 2\pi f_y$, given in Equation 4.4. In the approximation that all muons are at the magic $\gamma$, we set $a_\mu - 1/(\gamma^2 - 1) = 0$ in Equation 4.13 and obtain

$$\vec{\omega}_a \simeq \vec{\omega}_{diff} = -\frac{Qe}{m} \left[ a_\mu \vec{B} - a_\mu \left( \frac{\gamma}{\gamma+1} \right) (\vec{\beta} \cdot \vec{B}) \vec{\beta} \right]. \tag{4.21}$$

We adopt the (rotating) coordinate system shown in Figure 4.10, where $\vec{\beta}$ lies in the $yz$-plane, $z$ being the direction of propagation, and $y$ being vertical in the storage ring. Assuming $\vec{B} = \hat{y} B_y$, $\vec{\beta} = \hat{z}\beta_z + \hat{y}\beta_y = \hat{z}\beta \cos\psi + \hat{y}\beta \sin\psi$, we find

$$\vec{\omega}_a' = -\frac{Qe}{m}[a_\mu \hat{y} B_y - a_\mu \left( \frac{\gamma}{\gamma+1} \right) \beta_y B_y (\hat{z}\beta_z + \hat{y}\beta_y)]. \tag{4.22}$$

The small-angle approximation $\cos\psi \simeq 1$ and $\sin\psi \simeq \psi$ gives the component equations

$$\omega_{ay}' = \omega_a \left[ 1 - \left( \frac{\gamma-1}{\gamma} \right) \psi^2 \right] \tag{4.23}$$

and

$$\omega_{az}' = -\omega_a \left( \frac{\gamma-1}{\gamma} \right) \psi. \tag{4.24}$$

It is seen that the direction of $\vec{\omega}_a'$ in Figure 4.10 oscillates at the pitch frequency. We are interested in the overall precession rate about the y-axis, which can be obtained in terms of the period between the times that $\psi = 0$, or the average rate of precession during the pitch period. To facilitate obtaining this average, we project $\vec{\omega}_a'$ onto axes parallel and perpendicular to $\vec{\beta}$, using a standard rotation. Using the small-angle expansions $\cos\psi \simeq 1 - \psi^2/2$, and $\sin\psi \simeq \psi$, we find the transverse component of $\omega_a'$ is given by

$$\omega_\perp = \omega_{ay}' \cos\psi - \omega_{az}' \sin\psi \simeq \omega_a \left[ 1 - \frac{\psi^2}{2} \right]. \tag{4.25}$$

As can be seen from Table 4.1, the pitching frequency $\omega_y$ is more than an order of magnitude larger than the frequency $\omega_a$, so that $\omega_\parallel$ changes sign rapidly, thus averaging out its effect on $\omega_a'$. Therefore $\omega_a' \simeq \omega_\perp$,

$$\omega_a' \simeq -\frac{Qe}{m}a_\mu B_y\left(1 - \frac{\psi^2}{2}\right) = -\frac{q}{m}a_\mu B_y\left(1 - \frac{\psi_0^2 cos^2\omega_y t}{2}\right). \tag{4.26}$$

Taking the time average yields a pitch correction

$$C_p = -\frac{\langle\psi^2\rangle}{2} = -\frac{\langle\psi_0^2\rangle}{4} = -\frac{n}{4}\frac{\langle y^2\rangle}{R_0^2}, \tag{4.27}$$

where we have used Equation 4.6 $\langle\psi_0^2\rangle = n\langle y^2\rangle/R_0^2$. The quantity $\langle y_0^2\rangle$ was both determined experimentally and from simulations. For the 2001 period, $C_p = 0.27 \pm 0.036$ ppm, the amount the precession frequency is lowered from that given in Equation 4.5 because $\vec{\beta}\cdot\vec{B} \neq 0$.

We see that both the radial electric field and the vertical pitching motion *lower* the observed frequency from the simple difference frequency $\omega_a = (e/m)a_\mu B$, which enters into our determination of $a_\mu$ using Equation 3.23. Therefore our observed frequency must be *increased* by these corrections to obtain the measured value of the anomaly. Note that if $\omega_y \simeq \omega_a$ the situation is more complicated, with a resonance behavior that is discussed in References [6, 7].

## 4.5 Systematic Errors from the Pion and Muon Beamlines

Systematic effects on the measurement of $\omega_a$ occur when the muon beam injected and stored in the ring has a correlation between the muon's spin direction and its momentum. For a straight beamline, by symmetry, the averaged muon spin is in the forward direction for all momenta muons. However, muons born from pion decay in a bending section of the beamline will have a spin-momentum correlation, especially when the bend is used to make a momentum selection. This is illustrated in Fig. 4.11. For E821 we had a 32 degree bend with D1/D2 to select the pion momentum, and a 21 degree bend with D5 to select the muon momentum. 57% of the pions were still left at the latter bend. A plot of the simulated muon radial spin angle vs. momentum for the E821 beamline is shown in Fig. 4.12. The FNAL experiment beamline bends are given in Table 4.2.

Table 4.2: FNAL beamline horizontal bends.

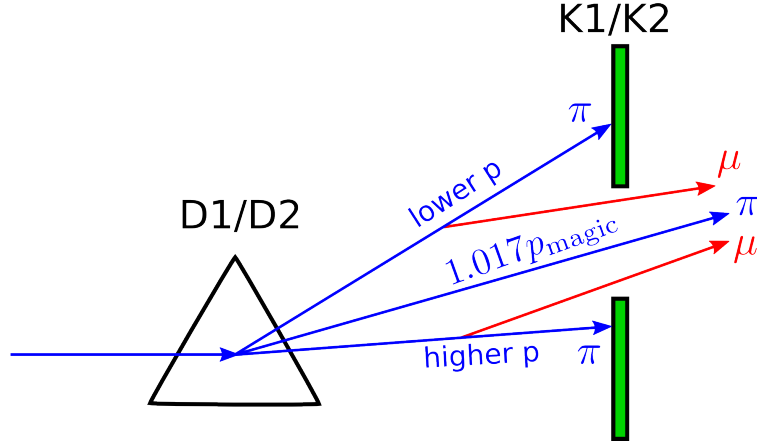| Bend | Pions left | $dp/p$ | Purpose |
|---|---|---|---|
| 3 degree | 96% | ±10% | Pion momentum selection |
| 19 degree | 41% | ±2% | M2 to M3 |
| Delivery Ring (DR) | 18% | ±2% | Remaining pions decay |
| After DR | $< 10^{-3}$ | ±1% | Muon momentum selection |

Figure 4.11: Cartoon of the E821 pion/muon beam going through D1/D2. The pions (blue arrows) with momentum (1.017±0.010) times the magic momentum pass through the K1/K2 collimator (green rectangles) slits. Some pions decay after the D1/D2 bend and the decay muons (red arrows) pass through the collimator slit. These muons may have approximately magic momentum, and finally are stored in the muon storage ring. The muon spin direction will then be correlated with it's momentum.
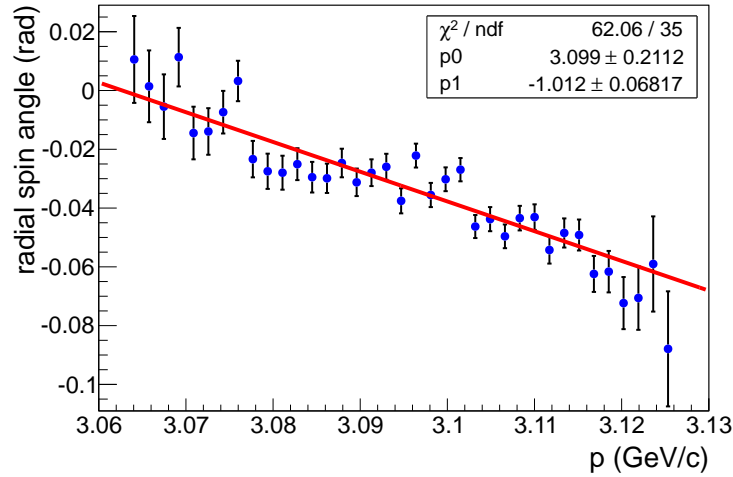


Figure 4.12: Simulation from Hugh Browns BETRAF program of the spin-momentum correlation of muons entering the E821 storage ring, i.e., at the end of the inflector magnet (symbols). The red line is linear fit to data points.

The systematic effect is calculated from:

$$\left\langle \frac{d\Theta_{\text{spin}}}{dt} \right\rangle = \left\langle \frac{d\Theta_{\text{spin}}}{dp} \frac{dp}{dt} \right\rangle \tag{4.28}$$

where $dp/dt$ occurs because the muon lifetime in the lab frame is gamma times the rest frame lifetime. This gave an E821 beamline "differential decay" systematic effect on the measurement of $\omega_a$ of 0.05ppm, which was sufficiently small for E821 that we didn't need to correct for it.

The design philosophy for the FNAL beamline is significantly different from that of E821. For E821 we had a beamline whose length was about the pion $\beta\gamma c\tau$, so to minimize the pion "flash" we selected $(1.017 \pm 0.010)$ times the magic momentum pions after the target and then selected $(1.0 \pm 0.005)$ times the magic momentum just before the muon storage ring. For the FNAL beamline, effectively all the pions will have decayed before the muon storage ring. The pion momentum selection right after the target is only a 3 degree bend and selects $\pm 10\%$ in momentum. The capture probability $Y_{\mu\pi}$ for the long straight section of the beamline is shown in Fig. 4.13. With $\pm 10\%$ momentum acceptance, the pions which are headed for the low momentum side of the beamline acceptance (see Fig. 4.11) can not give a magic momentum muon. The pions which are headed for the high momentum side of the beamline acceptance will be very inefficient in giving a magic momentum muon. Note that this is suggested by Fig. 4.13, but we haven't yet done the FNAL beamline simulation in the bending regions. For later bends, a larger fraction of the pions will have decayed prior to the bend compared to E821 (see Table 4.2). We believe this bending section of the beamline systematic error will be less or equal the E821 error, but we haven't properly simulated it yet. The time line for the simulation calculation is given in the next section.
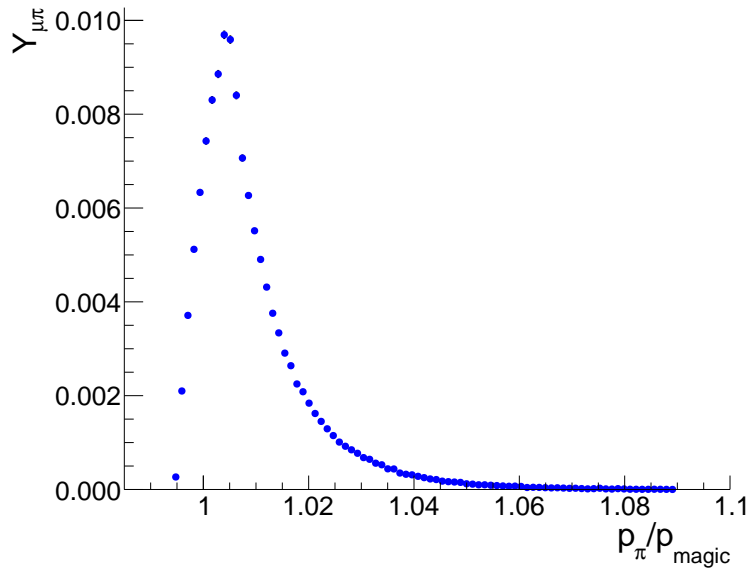


Figure 4.13: Parametric phase space calculation of the $\pi$-$\mu$ capture probability in the straight section of the FNAL pion decay channel. The muons have the magic momentum $\pm 0.5\%$.

Another systematic effect comes when the muons go around the delivery ring (DR). The cyclotron and anomalous magnetic moment frequencies are:

$$\omega_c = \frac{eB}{m\gamma} \qquad \omega_a \approx \frac{eaB}{m} \tag{4.29}$$

The former is exact while the latter is good to the sub-ppm level. The "spin tune" is then:

$$Q_{\text{spin}} = \frac{\omega_a}{\omega_c} \approx a\gamma \tag{4.30}$$

The spin-momentum correlation after seven turns in the DR, is shown in Fig. 4.14. The slope is less than the slope shown in Fig. 4.12. Of course, Fig. 4.14 is exact, but the energies of the muons in the storage ring are different from their energies in the DR due to the material the beam passes through between the DR and the storage ring. Once the simulation is complete, we will correct our measured value of $\omega_a$ for the beamline differential decay effect.
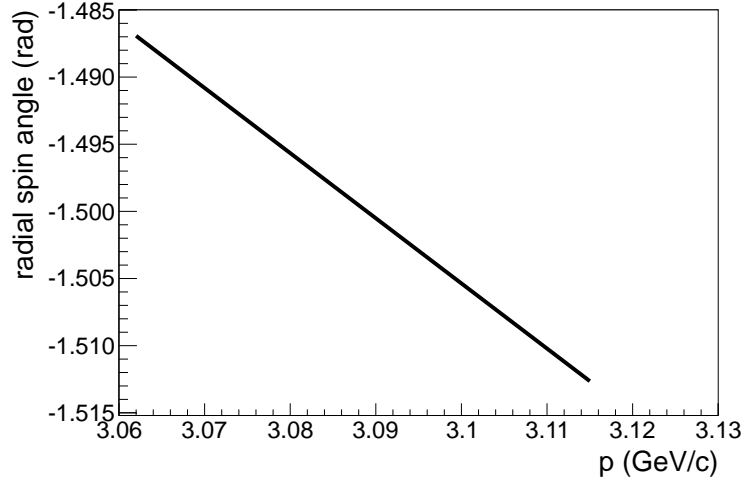


Figure 4.14: Radial spin angle vs. momentum after seven turns in the DR.

Such correlations also couple to the lost muon systematic error. For E821, the differential lost muon rate was about $10^{-3}$ per lifetime, while the differential decay rate was $1.2 \times 10^{-3}$ per lifetime. As discussed above, the FNAL differential lost muon rate will be less than $10^{-4}$ per lifetime.

## 4.5.1   Simulation plan and time line

We are planning to study the beamline systematic errors independently in two ways, using phase-space calculations and tracking. The phase-space calculations were first used by W.M. Morse for E821 [10]. In E989 the phase-space calculation were used to guide the design of the beamline [11] and to estimate the muon capture probability in the straight section for this document. While the phase-space method is approximation, it gives quick

insight into the problem and allows to make studies of an idealized beamline with required characteristics without having the actual design of the beamline.

For tracking calculations several off-the-shelf accelerator packages have been considered, `TRANSPORT`, `TURTLE`, `DECAY TURTLE`, `MAD`, `TURTLE with MAD input`. Suitable tracking program for $(g-2)$ must be capable of *i)* describing decay of primary particles (pions) into secondary particles (muons) and transporting the secondary particles and *ii)* transporting spin through the beamline. It turned out that none of the existing programs can be used "as is" for the studies of systematic errors in $(g-2)$. Some modification are needed of any of the existing programs. Lack of the source code in some cases (`DECAY TURTLE`) makes implementation of the missing features impossible. Our current plan for tracking simulations is to use the program `G4Beamline` for the following reason *i)* the program is well-supported and is under active development, *ii)* it is based on `Geant4` toolkit which is widely used in physics simulations, *iii)* spin tracking has been recently implemented in `Geant4`, *iv)* the accelerator team is planning to use `G4Beamline` for beamline simulations, therefore the input configuration file for the $(g-2)$ beamline will be provided by the experts, *v)* the common ground between `G4Beamline` and the downstream simulation program `g2RingSim` for the $(g-2)$ storage ring will simplify the task of combining the two programs together for back-to-back simulations.

Recently, a preliminary version of the `G4Beamline` for $(g-2)$ was released with significant boost in performance and bug fixes. The construction of the $(g-2)$ beamline model for `G4Beamline` is in progress. Basing on our experience, we expect to get the results from `G4Beamline` simulations in six months.

`G4Beamline` simulations for the straight section will be confronted with the phase space simulation to cross-check the two codes. In parallel, we are planning to extend the phase space method to the bending sections of the beamline (beamline elements with dispersion).

Finally, the production and collection of pions in the target station was simulated by `MARS` (see section 7.4.1). We are planning to confront `MARS` and `G4Beamline` simulations of the target station to cross-check the two codes.

### 4.5.2   Coherent Betatron Oscillation Systematic Error Simulations

The theory of coherent betatron oscillations (CBO) is given in the Beam Dynamics Section. Briefly, the E821 inflector was not well matched to the storage ring [12]. Furthermore, the E821 kicker did not provide the optimal kick. Large coherent betatron oscillations were observed in E821. These affect both the spin motion of the muon and the decay positron acceptance. Fig. 4.15 shows the spin precession from just the muon $g-2$, and the additional spin precession due to a fully coherent betatraon oscillation. The latter amplitude is $10^{-4}$ times the former. The CBO amplitude within the muon $dN/dt$ plot for each detector station is shown in Fig. 4.16. The E821 kicker had thicker plates than the E821 electric quads. The detectors shadowed by the kicker plates (detectors 7-9) had about twice the CBO amplitude compared to the detectors shadowed by the quad plates (4-6, 10-12, 16-18, and 22-24). The dominant CBO modulation effect seen in the muon $dN/dt$ plot is due to the decay positron acceptance. The E989 inflector and kicker teams are studying upgrades to the E821 design. The simulated CBO mean and width from a E989 kicker study with the E821 inflector is shown in Fig. 4.17. The E989 mean CBO modulation in this figure is about three times less
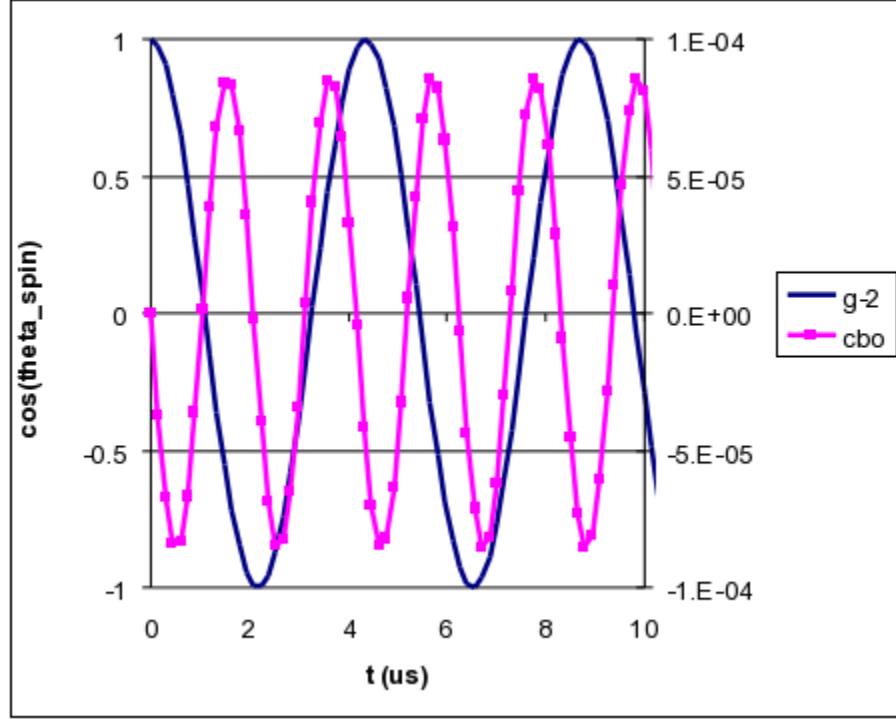
Figure 4.15: Spin precession from just the muon $g-2$ (lhs), and the additional spin precession due to a fully coherent betatraon oscillation (rhs).

than observed in E821. The E989 width modulation is about the same as observed in E821.

The muon $dN/dt$ multi-parameter function [12] is shown below. Fig. 4.18 show the effect of the CBO on the fitted muon $g-2$ frequency *vs.* the CBO frequency when equ. 4.31 was used to generate the data with the E821 parameters, but the fit was done with only the $V-A$ theory five parameters: $N_0$, $\tau_\mu$, $A$, $\omega_a$, and $\phi$. The E821 and E989 CBO frequencies are indicated. E989 will be 30% less sensitive to a given CBO modulation compared to E821 (2001 data). Since one never really understands systematic errors, our goal is to make all the beam dynamics systematic errors as low as reasonably achievable, i.e., zero, if possible.

The E821 muon $dN/dt$ analyzers found that the CBO de-coherence when fit to an exponential gave $\tau_{\mathrm{CBO}} \approx 0.1 - 0.14$ ms [12] for different running periods. Fig. 4.19 shows the fit to one of the running periods from 2001.

$$N(t) \;=\; \frac{N_0}{\gamma\tau_\mu} e^{-t/\gamma\tau_\mu} \cdot \Lambda(t) \cdot V(t) \cdot B(t) \cdot C(t) \cdot [1 - A(t)\cos(\omega_a t + \phi(t))] \qquad (4.31)$$

$$\Lambda(t) \;=\; 1 - A_{\mathrm{loss}} \int_0^t L(t) e^{-t/\gamma\tau_\mu} dt$$

$$V(t) \;=\; 1 - e^{-t/\tau_{\mathrm{VW}}} A_{\mathrm{VW}} \cos(\omega_{\mathrm{VW}} t + \phi_{\mathrm{VW}})$$

$$B(t) \;=\; 1 - A_{\mathrm{br}} e^{-t/\tau_{\mathrm{br}}}$$

$$C(t) \;=\; 1 - e^{-t/\tau_{\mathrm{CBO}}} A_1 \cos(\omega_{\mathrm{CBO}} t + \phi_1)$$
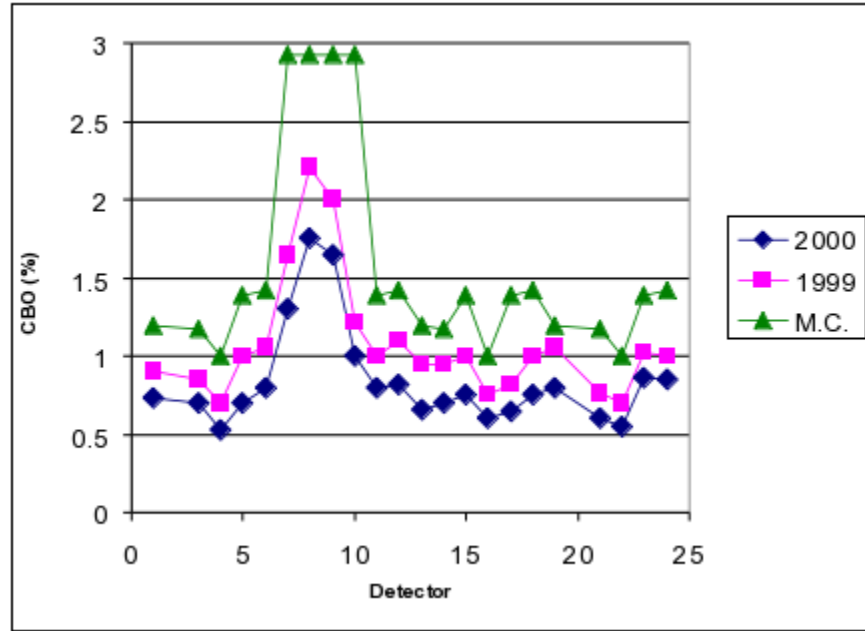
Figure 4.16: E821 observed and positron acceptance simulated CBO $A_1$ amplitudes vs. detector number. Detectors 7-9 were shadowed by the E821 kicker plates. The inflector angle was changed between the 1999 and 2000 runs.
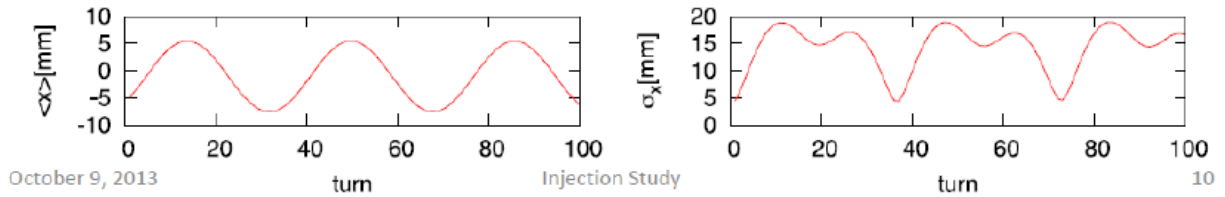


Figure 4.17: E989 kicker simulation showing the CBO modulation of the mean, and the width of the muon distribution vs. turn number [13]. The modulation of the mean is three times less than E821. The width modulation is about the same as E821.
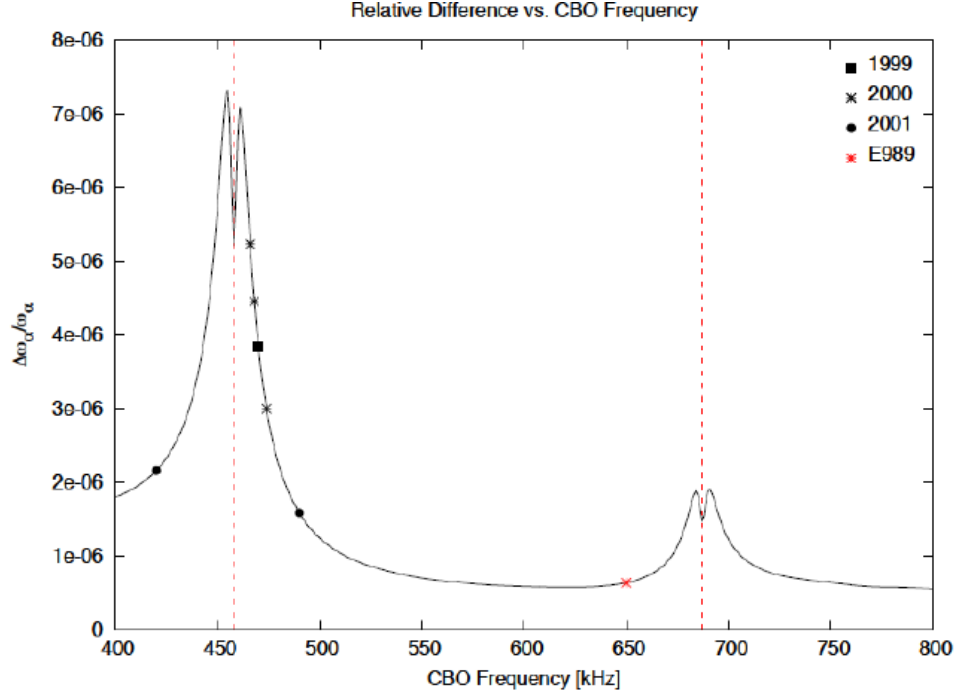
Figure 4.18: Effect of the CBO on the fitted muon $g - 2$ frequency vs. CBO frequency (see text for discussion). The E821 CBO frequencies and the planned E989 frequency are indicated.
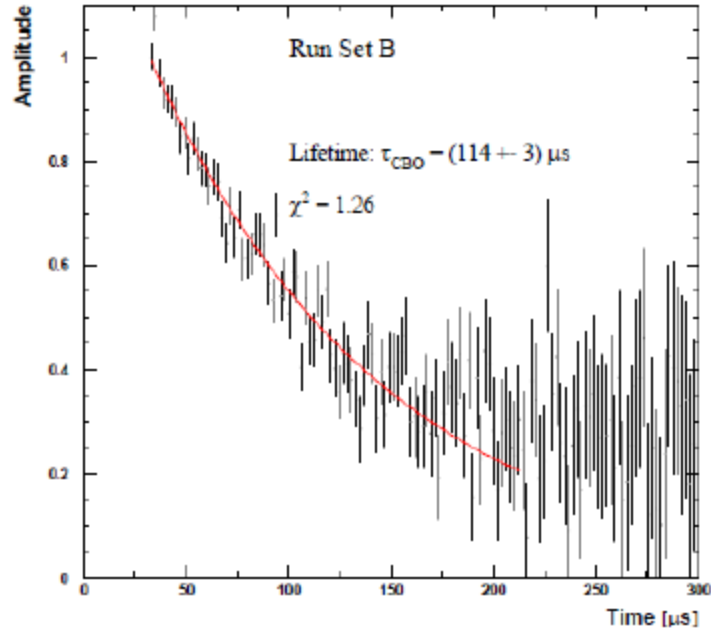


Figure 4.19: Time distribution of residuals from the 5-parameter fit at the CBO frequency for one set of E821 2001 run.
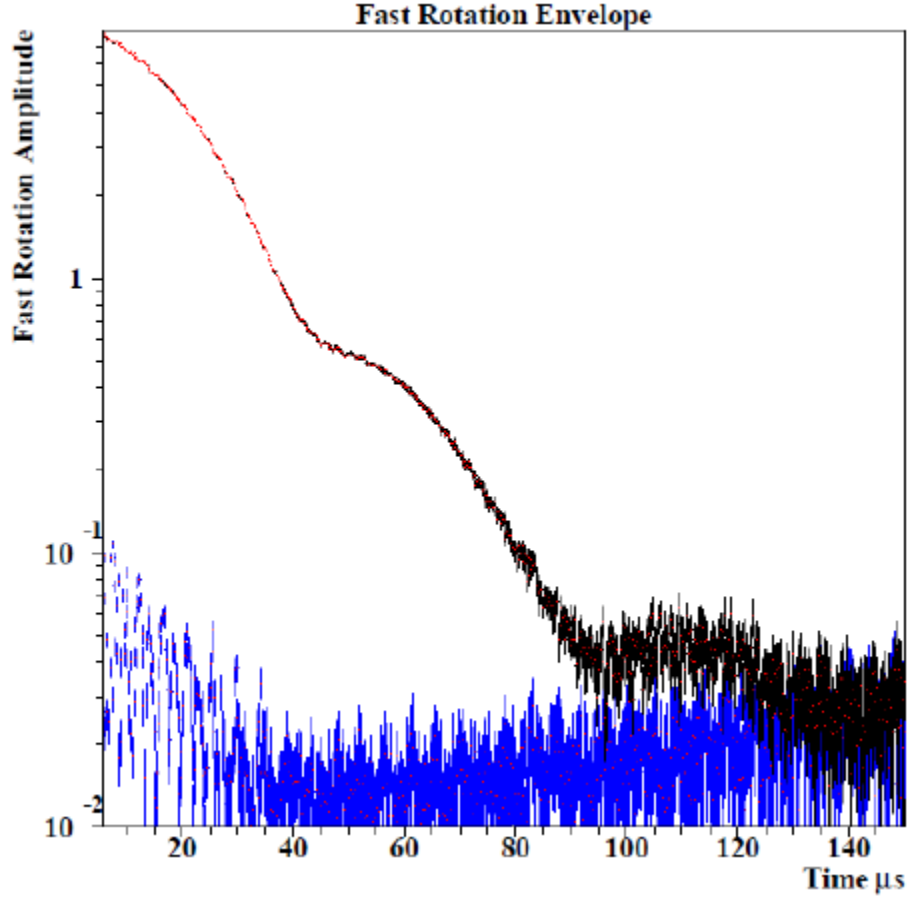
Figure 4.20: E821 de-coherence of the fast rotation envelope (red points with black statistical errors) from the 2000 run. Blue is after binning at the revolution period, before accidental overlaps were corrected.

$$A(t) = A\left(1 - e^{-t/\tau_{\text{CBO}}} A_2 \cos(\omega_{\text{CBO}} t + \phi_2)\right)$$
$$\phi(t) = \phi_0 + e^{-t/\tau_{\text{CBO}}} A_3 \cos(\omega_{\text{CBO}} t + \phi_3) \tag{4.32}$$

Next we discuss the calculation of CBO de-coherence, due to the muons having different beam dynamics frequencies.

$$f_{\text{CBO}} = f_{\text{rev}}(1 - Q_x) \tag{4.33}$$
$$\frac{df_{\text{CBO}}}{f_{\text{CBO}}} = \frac{df_{\text{rev}}}{f_{\text{rev}}} \oplus \frac{dQ_x}{1 - Q_x} \tag{4.34}$$

The E821 de-coherence of the revolution frequency is shown in Fig. 4.20. $df_{\text{rev}}/f_{\text{rev}} \approx 1.5 \times 10^{-3}$. From the muon $dN/dt$ plot fits, $df_{\text{CBO}}/f_{\text{CBO}} \approx 8 \times 10^{-3}$. This gives $dQ_x \approx 5 \times 10^{-4}$. This is the main source of the de-coherence of the coherent betatron oscillations.

Ref. [15] simulated the E821 2000 run CBO de-coherence due to the tune spread from the electric quadrpoles [14]. The simulated mean and width at the CBO frequency is shown
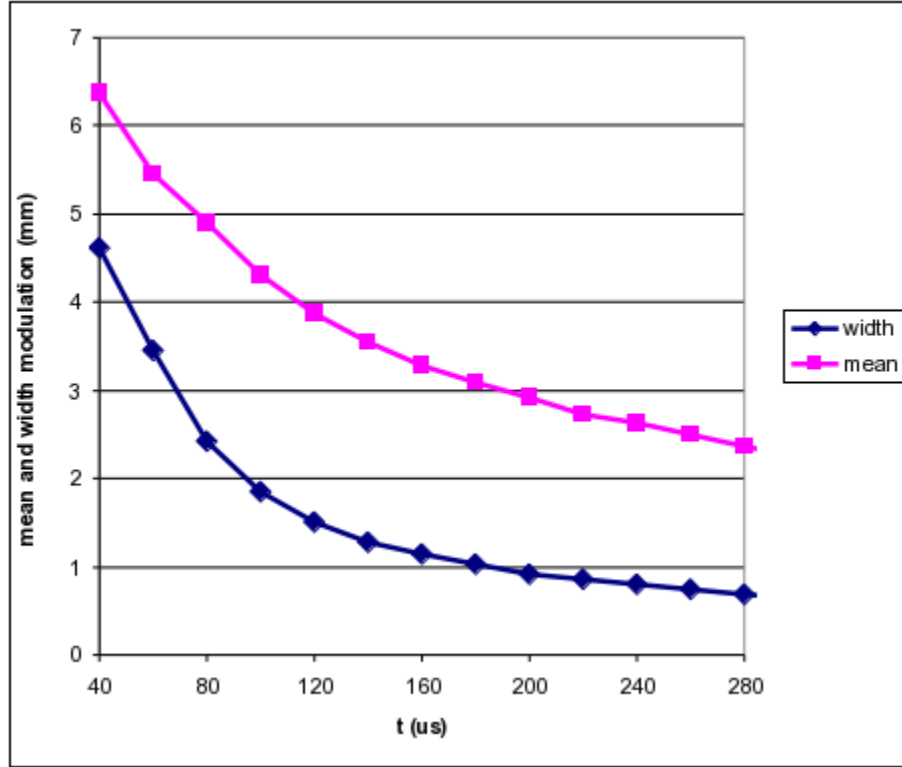
Figure 4.21: Ref. [15] horizontal mean and width modulation at the CBO frequency.

in Fig. 4.21. The mean had only the CBO frequency, but the width had both the CBO frequency, and twice the CBO frequency [12]. The muon $dN/dt$ plot had both the CBO frequency, and twice the CBO frequency. Ref. [15] then concluded that: "The beam width contributes 20-30% to the observed CBO signal for detectors 10-24 and starting at 25 $\mu$s". However, this logic is incorrect, as the CBO can have only the first harmonic, for example, but if the detector acceptance is non-linear vs. the betatron $x$-$x'$ oscillations, the other harmonics will appear in the muon $dN/dt$ plot. Nevertheless, Fig. 4.22 shows 70% mean and 30% width modulation (points labeled sum), and an exponential with $\tau = 114$ $\mu$s, which matches the Fig. 4.19 time distribution quite well. The fraction of the CBO modulation in the muon $dN/dt$ plot due to the mean, and the fraction due to the width will be determined in the simulation study. The CBO simulation will determine the E989 $C(t)$, $A(t)$, and $\phi(t)$ parameters for the kicker, quad, and free detectors, and the CBO systematic error for the $Q$ and $T$ methods of analysis.

### 4.5.3   Lost Muons

A systematic error occurs if the muons lost from the storage ring at late times have a different average spin direction compared to the stored muons. This difference in the spin direction occurs due to the production and storage processes. The E821 storage ring injection capture efficiency was $(4 \pm 1)$% [12]. Thus about 96% of the injected muons were lost. The E821 muon loss rate after 30 $\mu$s was lost/stored $\approx 10^{-3}$, or lost/injected $\approx 4 \times 10^{-5}$. Our goal is
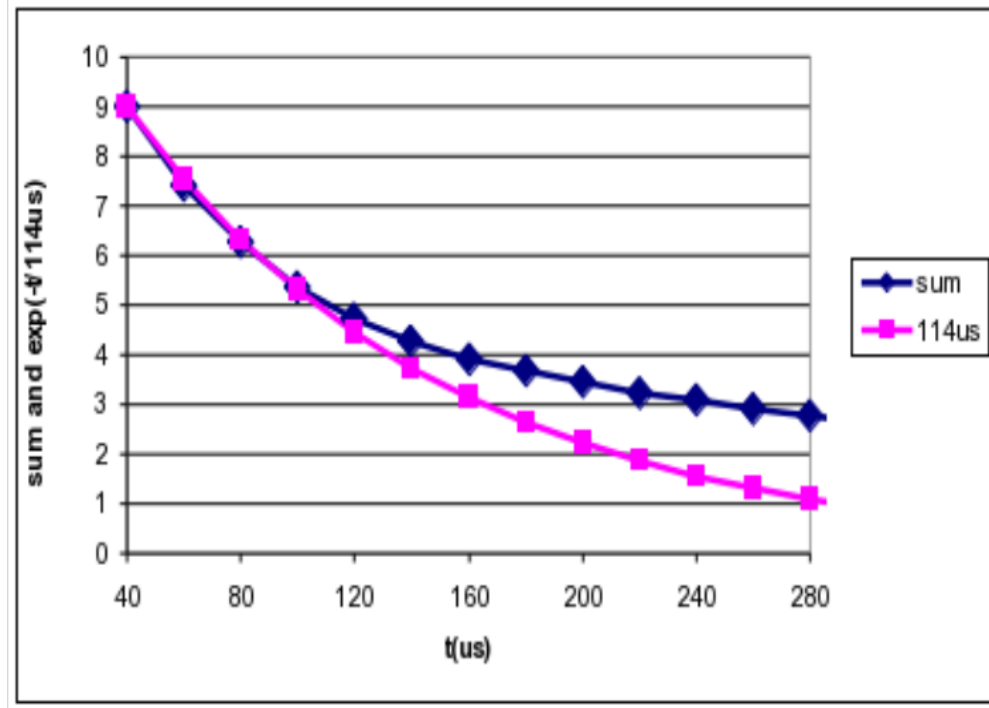
Figure 4.22: 70% mean and 30% width modulation (sum), and exponential with $\tau = 114\ \mu s$.

to reduce the lost muon rate after 30 $\mu$s by at least an order of magnitude compared to the E821 rate.

A schematic drawing of the E821 muon storage ring vacuum chamber is shown in Fig. 4.23. Some of the E821 full collimators were changed to 1/2-collimators, since the E821 kicker did not give an adequate kick for the first turn (see Kicker Section). For E989, all the collimators will be full collimators. The distortion of the closed orbit due to non-perfect magnetic fields, for uniform and perfect electric quads, is:

$$\Delta X_{\mathrm{e}}(\Theta) \quad \approx \quad \frac{R_0}{B_0} \sum_{N=1}^{\infty} \frac{B_{yNC}\cos(N\Theta) + B_{yNS}\sin(N\Theta)}{-N^2 + Q_x^2} \tag{4.35}$$

$$\Delta Y_{\mathrm{e}}(\Theta) \quad \approx \quad \frac{R_0}{B_0} \sum_{N=0}^{\infty} \frac{B_{RNC}\cos(N\Theta) + B_{RNS}\sin(N\Theta)}{-N^2 + Q_y^2} \tag{4.36}$$

$$\tag{4.37}$$

Fig. 4.24 shows the lost muon results of the E989 phase space model by a BNL high school summer student. One can readily see the effect a non-uniform magnetic field has on the muon losses. This study was limited by statistics, but the zero values for lost muons have at least a factor of ten fewer lost muons than E821 after 30 $\mu$s. However, this study assumed infinitely thick collimators, i.e., the muon was lost as soon as it hit a collimator. We next need a tracking study, including finite electric quads with non-perfect fields, following the muon after it first strikes the collimator, etc.
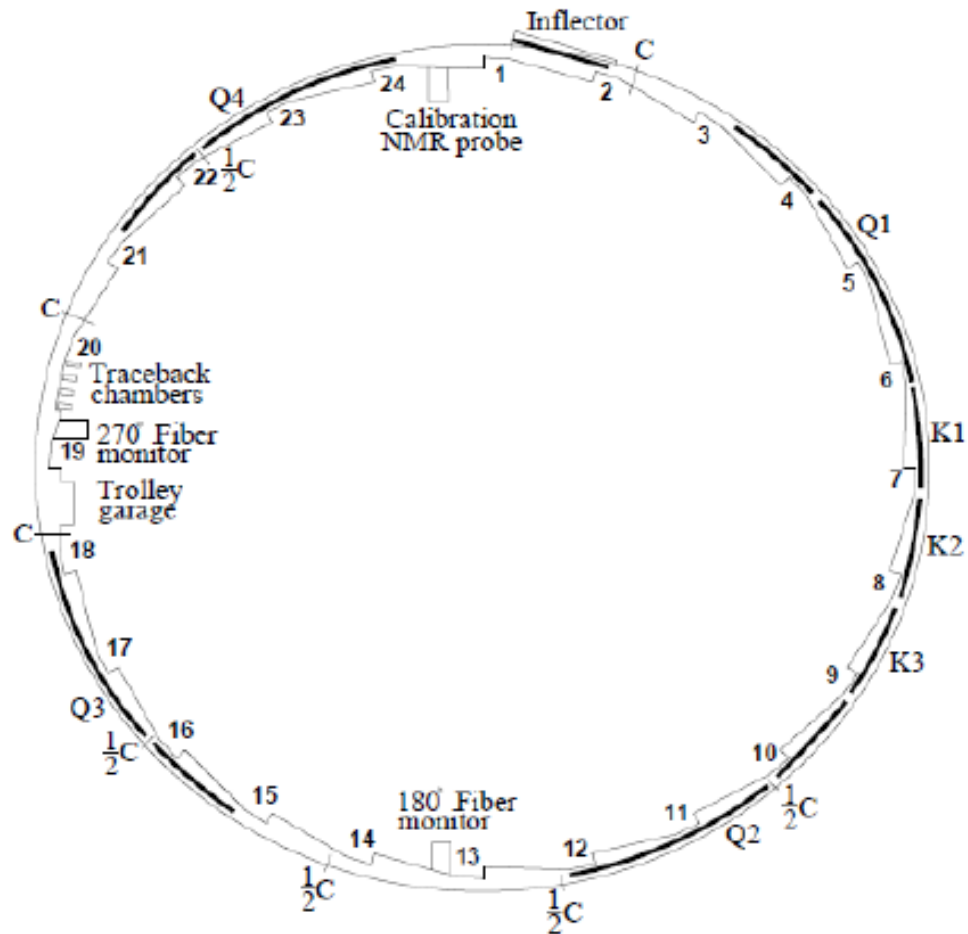
Figure 4.23: E821 vacuum chambers showing the locations of the electric quads and collimators.
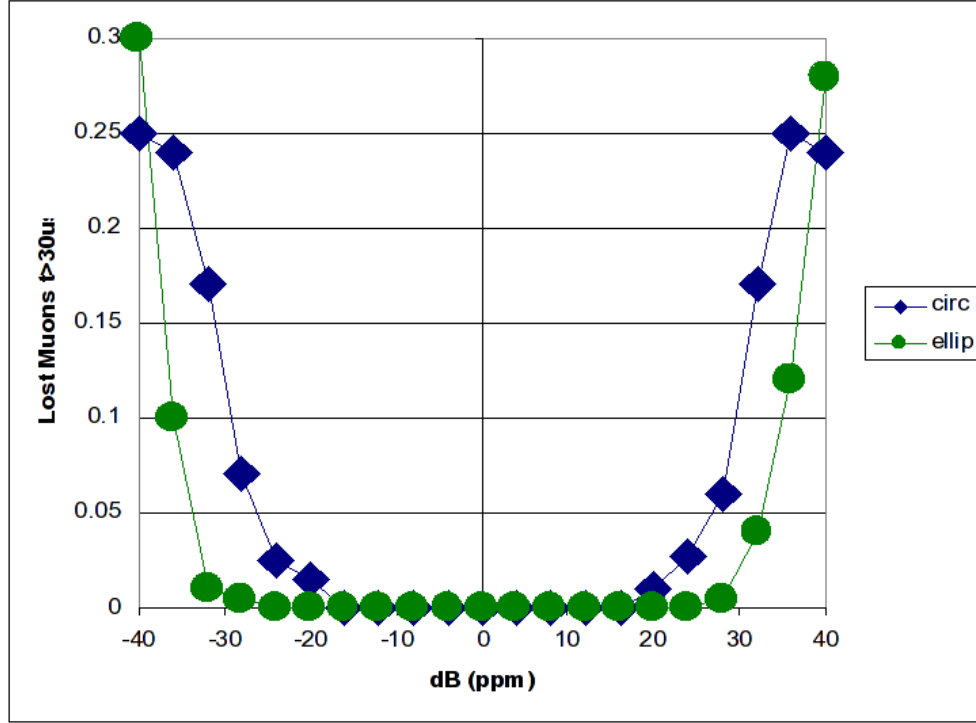
Figure 4.24: Lost muons after 30s from a phase space study vs. magnetic field uniformity, for both circular and elliptical collimators. Elliptical collimators follow $\sqrt{\beta_{x,y}}$.

## 4.5.4   Electric Field and Pitch Corrections

The theory of the electric and pitch corrections is given in the Beam Dynamics Section. The E821 electric field and pitch corrections to the anomaly were $(0.47 \pm 0.05)$ ppm and $(0.27 \pm 0.04)$ ppm, respectively. The table below gives more detail on the systematic errors.

| Systematic Effect | $E$ correction | Pitch |
|---|---|---|
| Difference Between Data and Simulation | $\pm 50$ ppb | $\pm 30$ ppb |
| Beam *vs.* Quad Electrode Position Uncertainty | $\pm 20$ ppb | $\pm 20$ ppb |

Our E989 goal is $< 30$ ppb for the electric field and pitch corrections combined. The electric field correction requires a precise knowledge of the momentum distribution of the stored muons. This is obtained by the so-called "fast rotation analysis", where the beam is observed to de-bunch as it rotates around the ring. The equilibrium closed orbit is given by:

$$x_{\mathrm{e}} = D \frac{dp}{p} \tag{4.38}$$

For E821 the head and the tail of the incoming bunch had identical momentum distributions. This will not be the acse for the E989 beam, since the beam goes around the Delivery Ring (DR) a number of times. The DR has $\langle D \rangle = 2$ m. Some pions decay to muons in the DR, so we have to track the pion momentum, which is higher than the muon momentum, and then the muon momentum. For muons which have five turns around the DR, for example:

$$\delta L \approx 10\pi(2\text{m})\frac{dp}{p} \approx 63\text{m}\frac{dp}{p} \tag{4.39}$$

$$\delta t \approx \frac{63\text{m}}{c}\frac{dp}{p} \approx 210\text{ns}\frac{dp}{p} \tag{4.40}$$

Putting in $dp/p$ of several parts per thousand shows that this will be a small effect, but it will be studied in the simulation.

### 4.5.5 Collimator Study

The E821 collimators were IR = 45 mm, OR = 55 mm, and thickness 3 mm Cu [12]. The E821 collimator design was based on a "back of the envelope" calculation. For E989 we need a real simulation to minimize the lost muon systematic error, maximize the positron detection, and allow adequate space for supplementary detectors.

### 4.5.6 Simulation Responsibilities and Schedule

Each calculation listed needs to be done independently by at least two different people, or by one person but with a different method, i.e., analytical calculation, phase space simulation, tracking simulation, etc. BDT = Beam Dynamics Team (BNL, FNAL, Univ. Mississippi, and CAST, Korea). The dates shown are estimates of when the simulation studies will be completed by calendar year and quarter.

**Differential decay  Q2 2015**

1. Kicker – BDT
2. Muon spin in DR – BDT
3. Pion decays in bends – BDT
4. Straw system – Detector Team

**CBO  Q3 2015**

1. $F(t)$ for the de-coherence – BDT
2. Kicker plate study – BDT
3. Effect on E989 $\omega_a$ for $Q$ method – BDT
4. Effect on E989 $\omega_a$ for $T$ method – BDT
5. Straw system/fiber beam monitor system – Detector Team
6. Hardware CBO damping – BDT

**Lost muons  Q1 2015**

1. Phase space – BDT

2. Tracking – BDT

3. New "scraping" hardware? – BDT

## Collimators (analytical, phase space, tracking)  Q1 2015

1. Number and Thickness – lost muon study – BDT

2. Number and Thickness – decay positron study – Detector Team

## Pitch Correction  Q2 2015

1. Straw system/fiber beam monitor system – Detector Team

2. Beam Dynamics – BDT

## E field Correction  Q2 2015

1. Fast rotation – BDT

2. Beam Dynamics – BDT

## Distortion of closed orbit due to non-perfect electric quad fields  Q2 2014- Finished [17]

1. Analytical calculation – BDT

2. Tracking – BDT

## Distortion of closed orbit due to non-perfect magnetic fields  Q2 2014 - Finished [18]

1. Analytical calculation of effect on average magnetic field – BDT/Magnetic Field Team

2. Tracking – BDT

## Geometric Phase  Q2 2014 - Finished [16]

1. Analytical calculation – BDT

2. Tracking – BDT

# References

[1] H. Wiedemann, *Particle Accelerator Physics* Vol. 1, Springer-Verlag, (1993) p. 54.

[2] D.A. Edwards and M.J. Syphers, *An Introduction to the Physics of High Energy Accelerators*, John Wiley & Sons, (1993) p. 75.

[3] F. Combley and E. Picasso, Phys. Rept. **14**, 1 (1974).

[4] We follow the approach given by J.M. Paley, Ph.D. Dissertation, Boston University, 2004.

[5] L.H. Thomas, Nature **117**, (1926) 514 and Phil. Mag. **3** (1927) 1, Bargmann V, Michel L, Telegdi VL, Phys. Rev. Lett. 2:435 (1959)

[6] F.J.M. Farley and E. Picasso, in Quantum Electrodynamics, Adv. Series on Dir. in H.E.P., V7, T. Kinoshita, ed., World Scientific, 479, (1990).

[7] F.J.M. Farley, Phys.Lett. **B 42**, 66 (1972), and J.H. Field and G. Fiorentini, Nuovo Cimento, **21 A**, 297 (1974).

[8] Y. Orlov, et al., Nucl. Instrum. Meth. **A482**, 767 (2002).

[9] P. Debevec, Ringbeta, DocDB document #762.

[10] B. Morse, Phase Space Calculations of Muon Injection, Brookhaven National Laboratory, 1998, (g-2) note #303, 1998.

[11] V. Tishchenko and W.M. Morse, Phase-Space Calculations of the Muon Acceptance by the Straight Section of the Fermilab Beamline, Brookhaven National Laboratory, docdb #487, 2012.

[12] G. Bennett et al., Phys. Rev. 73, 072003 (2006).

[13] T. Gadfort, ELOG 183 (2013).

[14] Y. Semertzidis et al., Nucl. Inst. Meth. A303, 458 (2003).

[15] R. Prigl et al., g-2 note 427 (2002).

[16] V. Tishchenko et al., "Geometric Phase Systematic Error", DocDB document #1819.

[17] V. Tishchenko et al., "Quads update", DocDB document #1750.

[18] J. Grange, "Field analysis update", DocDB document #1452.